Article:
Tu, J., Chen, X. B., Ruan, X. Z. et al. (10 more authors) (2020) Direct observation of hidden spin polarization in 2H-MoT e2. Physical Review B. 035102. ISSN 2469-9969

https://doi.org/10.1103/PhysRevB.101.035102

Direct observation of hidden spin polarization in 2H-$MoTe_2$

J. Tu[1+], X. B. Chen[2+], X. Z. Ruan[1*], Y. F. Zhao[1], H. F. Xu[1], Z. D. Chen[1], X. Q. Zhang[1], X. W. Zhang[2*], J. Wu[3], L. He[1], Y. Zhang[4], R. Zhang[1], Y. B. Xu[1,3*]

[1]Jiangsu Provincial Key Laboratory of Advanced Photonic and Electronic Materials, Collaborative Innovation Center of Advanced Microstructures, School of Electronic Science and Engineering, Nanjing University, Nanjing, 210093, China.

[2]Shenzhen Key Laboratory of Flexible Memory Materials and Devices, College of Electronic Science and Technology, Shenzhen University, Nanhai Ave. 3688, Shenzhen, Guangdong 518060, China.

[3]York-Nanjing Joint Center in Spintronics, Department of Electronic Engineering and Department of Physics, The University of York, York, YO10 5DD, United Kingdom.

[4]Central Laser Facility, STFC Rutherford Appleton Laboratory, Didcot OX11 0QX, United Kingdom.

+These authors contributed equally to this work.

*Correspondence and requests for materials should be addressed to Y.B.X. (email: ybxu@nju.edu.cn) or to X.Z.R. (email: xzruan@nju.edu.cn) or to X.W.Z. (email: xiuwenzhang@szu.edu.cn).

Abstract:

Centrosymmetric (CS) non-magnetic materials with hidden spin polarization induced by non-CS site symmetries and spin-orbit coupling are promising candidates for spintronic applications, in light of the zero net spin polarization and modulatable spin effects hidden in the local structures. There is, however, an open issue regarding the possible spin splitting induced by broken inversion symmetry at the sample surface. Here, we performed combinatorial experimental and theoretical studies on the potentially hidden spin polarization in 2H-$MoTe_2$ and its mechanism. A large spin splitting of 236meV and opposite spin polarizations up to 80% along out-of-plane

direction (z-axis) in K and K′ valleys were observed from both spin- and angle-resolved photoemission spectroscopy (spin-ARPES) and density functional theory (DFT). We further found from the DFT calculations that a medium dipole field mimicked the surface symmetry breaking in ARPES measurements induces negligible variation of spin polarization. Our study demonstrates the existence of the intrinsic hidden spin effects in 2H-$MoTe_2$ and opens a way of utilizing these effects in spintronic devices.

I. INTRODUCTION

Spin polarization in non-magnetic materials originates from the break of inversion crystalline symmetry [1-5] that could occur globally [1,2] or locally [3-6]. Such spin polarization can induce an effective magnetic field [7] for operating electron's spin in the absence of magnetic ions or field. At the same time, two-dimensional transition metal dichalcogenides (TMDCs) are promising materials for new-generation electronic devices with several virtues including direct band gap [8-12], superconductivity [13,14], ideal Van der Waals heterostructures [15], and valleytronics [15-18]. Spin splitting [19-22] has been observed in the K valley of inversion asymmetric TMDC structures that are interlocked [14,23,24] with the coexisted valley polarization effect [16-18]. Whereas in the centrosymmetric TMDC structures, a new type of spin effect, i.e. the hidden spin polarization [5], also known as layer-locked hidden spin texture in layered materials [3], has been observed [4,25-28]. Although it is well established that the optical properties of inversion symmetric TMDC systems [29-31] are qualitatively affected by their hidden spin texture, a concern that the observed hidden spin texture [4,25-28] might be mainly induced by the broken inversion symmetry in experiments was raised recently [32]. Therefore, it is critical to perform combined experimental and theoretical studies on centrosymmetric TMDC materials such as 2H-$MoTe_2$ to explore the mechanism of the hidden spin polarization [5].

$MoTe_2$ possesses intriguing physical properties, including type-II topological Weyl semimetal phase [33], spin splitting [28], and valleytronics [34]. It can be stabilized near room temperature in three types of crystal structures, namely the 2H

(hexagonal) [35], 1T′ (monoclinic) [36], and T_d (orthorhombic) [33] phases. The tunability of crystal structures (from 2H to 1T′ [35] and from 1T′ to T_d-$MoTe_2$ [28]) and the corresponding physical properties in $MoTe_2$ offers an opportunity to build ohmic homojunction contact [37], making it an ideal platform for two-dimensional electronic devices. Here, we focus on the spintronic properties of the highly symmetrical semiconducting phase of $MoTe_2$, i.e. the centrosymmetric hexagonal 2H phase with potentially hidden spin polarization. By using spin-ARPES, we observed strong net spin polarizations on the surface of 2H-$MoTe_2$, which have opposite polarization directions in the K versus K′ valleys of the hexagonal lattice. We tested the two possible origins of the measured spin polarization via combinatorial theoretical and experimental studies: (i) the weak surface dipole field due to the breaking of bulk inversion symmetry, and (ii) the layer-locked hidden spin polarization. We find that the evaluated spin texture (polarization directions) in the situation with broken symmetry in the appearance of a medium surface dipole field are analogous to that in the centrosymmetric structure. For both cases, the calculated spin polarizations are nearly identical and both agree well with the measured spin polarization. This shows that the contribution of the symmetry-breaking surface dipole field to the measured spin polarization is negligible. Our combined experimental and theoretical studies thus reveal the existence of the intrinsic hidden spin polarization in centrosymmetric materials.

II. EXPERIMENTAL DETAILS

2H-$MoTe_2$ sample was synthesized by the CVT method. High purity Mo and Te powders were mixed with mole ratio in a quartz tube. Under the pressure less than 0.1 Pa, the tube was heated to 700℃ within 12 hours, maintained at this temperature for 3 days and then cooled down to room temperature within 12 hours, to get $MoTe_2$ polycrystalline powder. $TeCl_4$ powder was used as the transporting agent to be mixed with $MoTe_2$ powder in a new quartz tube. The tube was heated to 1040℃ within 2 hours, maintained for 5 days, and then cooled down to room temperature within 12 hours, yielding 2H-$MoTe_2$ single crystal.

The ~~E~~electronic band structure measurements were conducted on ARPES system~~,~~ with a~~the~~ SPECS PHOIBOS150 hemispherical energy analyzer ~~of that is SPECS PHOIBOS150~~. The ~~B~~base pressure of the analyzer chamber is 2×10^{-10} mbar. A helium lamp is used to generate ultraviolet photons with an energy of 21.218 eV (He-I). The angular resolution of the system is ±0.05° and the energy resolution is 35 meV at room temperature. The sample was cleaved in situ in an ultra-high vacuum chamber (4×10^{-8} mbar) by using a scotch tape to obtain clean surface. Spin detection is realized by ~~use~~using ~~of~~ a Micro-Mott spin detector that includes a strong spin-orbital coupling target (thorium, Au? Need to check), and four channel electron multipliers to collect the scattered electrons. A small circular aperture is chosen to confine the photoelectrons from the same point of reciprocal space.

III. EXPERIMENTAL RESULTS

Figs. 1(a) and 1(b) display the lattice structure of 2H-$MoTe_2$ (space group: $P6_3/mmc$) on top and side views, respectively. Fig. 1(c) shows the Brillouin zone of 2H-$MoTe_2$ in reciprocal space. The molybdenum layer is sandwiched between two layers of tellurium within one monolayer, and each atom is surrounded by three atoms of another type ~~on top view~~. The Te-Mo-Te slabs are bonded with each other by Van der Waals forces by the stacking pattern shown in Fig. 1(b). The planar structures of up and down monolayers are related to each other by a rotation of 180°, constituting an inversion symmetric unit cell. It crystallizes in a trigonal prismatic arrangement with an in-plane lattice constant of 3.517 Å and an out-of-plane lattice constant of 13.962 Å [38] . ~~By use of a laser with wavelength of 514nm,~~ Raman spectrum measured with a laser of the wavelength of 514nm, under normal pressure and room temperature, is included in Fig. 1(d), which ~~–~~demonstrates two phonon oscillation modes, A_{1g} at 172.65 cm^{-1} and E^1_{2g} at 233.15 cm^{-1}, corresponding to the characteristic out-of-plane and in-plane phonon modes, respectively. The crystal structure of 2H-$MoTe_2$ was investigated using high-resolution X-ray diffraction (XRD) with Cu Kα radiation (λ=1.5418 Å). Fig. 1(e) presents the result of the XRD out-of-plane θ-2θ scan for the 2H-$MoTe_2$ sample. A group of diffraction peaks are clearly observed at 12.94, 25.74, 38.88 and 52.58 degree, which are corresponding to the (002), (004), (006), (008) plane of 2H-$MoTe_2$, respectively [39].

Fig. 2(a) shows the valence band structure along M-K-Γ-M [Fig. 1(c)] at room temperature. The valence band maximum of 2H-$MoTe_2$ at K and Γ are ~~very~~ rather close to each other, which is much different from MoS_2 [8] and $MoSe_2$ [40]. ~~That is an~~ This

will be an advantage for the applications in the field of hole-type spin based devices [41]. Band structure along K-Γ-K′ (see Fig. S1 [42]) reveals symmetry pattern except for the different intensitiesy along two directions, simply because of the photoemission matrix element effects. The band splitting at K point is 236 meV, as shown in Fig. 2(b), which is larger than that of MoS_2 and $MoSe_2$, implying more intense stronger spin-orbit interaction. We will prove that the symmetric valleys locating at K and K′ have inverse spin polarizations within each monolayer.

The energy distribution curves (EDC) at K and M point are shown in Figs. 2(b) and 2(c), respectively. One can clearly see that there are two energy distribution peaks corresponding to the first and second valence bands at K point. There is a Hugelarge splitting of 236 meV between two peaks in the EDC curve around K valley is obvious as shown clearly in Fig. 2(b). The EDC at K′ is identical to that at K point. Fig. 2(c) demonstrates that the peaks become broadening at M point. The measured spin polarizations around K (K′) and M are shown in Figs. 2(d) and 2(e), respectively. Since the escape depth of photoelectrons from K (K′) valley is about 6 Å with the photon energy of 21.218 eV [43], which is less than the out-of-plane lattice constant 13.962 Å, most photoelectrons come from the first layer. Therefore, the spin polarization results basically should represent the topmost monolayer with very small little contributions from the lower layers.

The spin polarizability detected by spin-ARPES is defined as:

$$P = \frac{1}{S_{eff}} \frac{I_+ - I_-}{I_+ + I_-} \quad (1)$$

The value of S_{eff} is 0.16±0.01, which is the effective Sherman function determined by the spin-ARPES system. I_+ and I_- are the intensity acquired by the two channeltrons at opposite directions. Spin polarizations at K and K′ are demonstrated in Fig. 2(d). The polarization at K is opposite to that at K′ with the same level, verifying the completeness of time reversal-symmetry and no net magnetic momentum existings. The large spin polarization of 80% at K and K′ has proven pure spin splitting at these two valleys, coinciding with type II Dresselhaus effect [5]. In-plane spin polarization data at K and K′ are shown in Fig. S2 [42], which demonstrate negligible spin polarization. Considering the geometry of the system as shown in Fig. S3 and non-polarized photons used during spin-ARPES measurements ~~as shown in Fig. S3~~ [42], the influence to the spin polarization vertical to the sample surface due to the matrix element effect [44,45] (check refs) can be estimated to be around 6-12%, ~~is negligible compared to 80% [44,45].~~ which is much smaller compared to the spin polarization of 80% observed. Therefore, the spin polarization detected represents the intrinsic spin polarization at K and K′. The detected spin polarization should ~~is~~ also be domain influenced. As ~~we~~ discussed before, different sectors (α, β) can induce reverse spin polarization, which is also indicated in [4]. Hence, the terminal sector of the sample can ~~also~~ influence the results. In this work, the helium light source was focused on the same location of the sample surface during the spin-ARPES measurements to minimize any possible influence induced by domain. ~~Since the~~ The large ~~huge~~ spin ~~splitting~~ polarization of up to 80% acquired at K and K′ indicates that ~~, we can conclude that~~ the domain detected is mainly terminated with one sector. ~~, and we kept the focus spot of the helium lamp at~~

~~the same location during the spin-ARPES measurements to avoid the influence induced by domain.~~ However, with the breaking of inversion symmetry at sample surface, vertical dipole in 2H-$MoTe_2$ could be another cause of the observed spin polarization. No net spin polarization exists at M point, as shown in Fig. 2(e), ~~which means~~ suggesting that the spin polarized states are also regulated in momentum space, coinciding with the results of WSe_2 [29]. The large spin polarization ~~data above~~ observed experimentally ~~reveals~~ demonstrates that there exists inverse net spin splitting around K and K′ valleys, indicating the inequivalence of the two valleys within ~~each monolayer (here predominately,~~ the topmost monolayer~~)~~.

IV. DFT CALCULATIONS

To reveal the origin of the above measured spin splitting, we conducted theoretical evaluations on the electronic structure and spin polarization of 2H-$MoTe_2$ in the framework of DFT [42]. Fig. 3(a) shows the calculated orbital-projected band structure of bulk 2H-$MoTe_2$, illustrating that the majority components of the first two valence bands (VB1 and VB2) at K valley are Mo-*d* states. The experimentally measured valence band structure [Fig. 2(a)] is rather similar to the calculated valence band of bulk materials, indicating that the surface effect in experiments is ignorable. The calculated energy difference between VB1 and VB2 at K valley of 2H-$MoTe_2$ is 283 meV, slightly higher than the experimental value of 236 meV, but smaller than the measured spin splitting in WSe_2 [4], suggesting that the spin splitting is mainly related to the M site in

MX_2 (W has larger SOC than Mo whereas Se has smaller SOC than Te). We further project the spin and orbital components of VB1 and VB2 at K valley to illustrate the segregation of spin states. As shown in Figs. 3(b) and (c) for the majority orbital (Mo-$d_{x^2-y^2}$ state), the spin up (down) states are segregated in the β (α) sector for VB1 at K point, whereas for VB2, the spin up (down) states are in α (β) sector, demonstrating a case of spin-layer locking. Fig. S4 [42] shows that the states at K′ point have the opposite spin-polarization directions as the corresponding states at K point, which could be related to the experimentally observed opposite spin polarizations at K and K′.

To clearly demonstrate the relationship between the experimentally measured net spin polarization and the potentially hidden spin polarization in $MoTe_2$ as ~~(~~anticipated from its crystalline symmetry [5]~~)~~, we evaluate the local spin polarizations of the inversion-symmetric α and β sectors in bulk 2H-$MoTe_2$, as shown in Figs. 4(a) and 4(b). The local spin polarizations of each sector is calculated by summing the expectation values of spin operator over the subspace of degenerated states, as the energy bands in 2H-$MoTe_2$ are doubly degenerated per time reversal symmetry and inversion symmetry, thus the evaluated local spin polarization [5] is gauge invariant. As the VB1 and VB2 states measured in experiments are mainly from Mo atoms, we will focus on the symmetry of Mo sites and its related spin polarization. In each 2H-$MoTe_2$ layer (α or β sector), the inversion-asymmetric point group D_{3h} of Mo sites leads to local Dresselhaus spin polarization, as shown by red (blue) arrows for α (β) sector in Figs. 4(a) and 4(b). ~~a~~All the spin polarizations are along out-of-plane directions without helical spin texture, confirming that the spin effects are dominantly related to the Mo sites. The two

layers (α and β sectors) in the primitive cell [Fig. 1(b)] possess opposite local spin polarizations, leading to compensated Dresselhaus spin polarization. Although the Te sites in 2H-$MoTe_2$ with C_{3v} point group symmetry could introduce Rashba spin polarization [5], their effect is negligible for VB1 and VB2 at K (K′) valley.

The net spin polarization observed in our experiments is ~~a combination~~ the sum ? of the local spin polarization of the 2H-$MoTe_2$ layers with a set of weights that break the full compensation of local Dresselhaus effects, ~~the~~where the weights are related to the escape depth of photoelectrons. Fig. 4(c) shows the spin polarizations (S_z) evaluated from the spin polarization data of α and β sectors shown in Figs. 4(a) and 4(b) for VB1 and VB2, considering the escape depth of photoelectrons [43]. We find that the spin polarizations of VB1 at K (K′) are along $-z$ (z) direction, whereas those for VB2 are along z ($-z$) direction, in agreement with experimental results [Fig. 2(d)]. Both experiment and theory ~~find~~ suggest nearly vanished spin polarization at M point.

To test the effect of surface symmetry breaking in experiments, we have ~~appl~~applied~~y~~ a medium dipole field of 50 kV/cm (considering the medium breakdown field of $MoTe_2$) along z direction in the 2H-$MoTe_2$ structure and calculated the spin polarization of the inversion asymmetric case, as shown in Figs. 5(a)-5(d). In the presence of dipole field, the doubly degenerate VB1 (VB2) band splits into singly degenerated $VB1_a$ and $VB1_b$ ($VB2_a$ and $VB2_b$) bands, and each possesses a net spin polarization as demonstrated by the violet arrows. The band structure of 2H-$MoTe_2$ under dipole field is shown in Fig. S5 [42], demonstrating negligible band splitting induced by the dipole field. ~~t~~There is also no visible surface-symmetry-breaking

induced band splitting in the experimentally measured band structure [Fig. 2(a)]. After consideration of the escape depth of photoelectrons, we obtained the spin polarization (S_z) data in bulk 2H-$MoTe_2$ under dipole field [Fig. 5(e)], using the same method as for Fig. 4(c) by decomposing the spin polarization onto the two $MoTe_2$ monolayers in the unit cell. We find that the results in Fig. 5(e) are almost identical with those in Fig. 4(c), ~~indicating~~ confirming that the effect of dipole field mimicked surface symmetry breaking is negligible. We would like to note that, ~~F~~for other material systems with strong surface symmetry breaking effect or large surface dipole field, one can determine the contributions from bulk hidden spin polarization versus surface symmetry breaking by comparing the calculations with [e.g. Fig. 5] or without [e.g. Fig. 4] dipole field. The surface dipole field and the bulk hidden spin polarization can also induce different fingerprints in spin texture, e.g. helical versus non-helical spin texture.

V. CONCLUSION

In summary, we have performed spin-ARPES measurements and first principle evaluations of the spin polarization in 2H-$MoTe_2$ and ~~,~~ reveal~~ing~~ a hidden Dresselhaus spin polarization~~s~~ in the K and K′ valleys ~~that have~~ with opposite spin texture~~s~~. Our detailed calculations ~~We~~ demonstrate that the effect of symmetry-breaking surface dipole field on spin polarization in the surface sensitive measurements is rather weak as indicated by its negligible contribution to the measured spin polarization and the invisible splitting of energy bands. This shows that the measured spin effects ~~mainly~~

originate from the intrinsic hidden spin polarization in the bulk phase. The large spin splitting and net spin polarization found in spin-ARPES experiments also suggest that the hidden spin effects in inversion symmetric layered compounds can be used to generate large spin splitting on the surfaces in the absence of strong dipole field. Our combinatorial experimental and theoretical studies clarify the existence of hidden spin polarization in the centrosymmetric materials and opens the way of designing novel functional materials with coexisting hidden spin polarization and other hidden effects, such as hidden orbital polarization [46] and hidden Berry curvature [47], for the energy efficient spintronics applications.

References

[1] G. Dresselhaus, Phys. Rev. **100**, 580 (1955).

[2] E. I. Rashba, Sov. Phys. Solid State **2**, 1109 (1960).

[3] J. Schaibley and X. Xu, Nat. Phys. **10**, 798 (2014).

[4] J. M. Riley, F. Mazzola, M. Dendzik, M. Michiardi, T. Takayama, L. Bawden, C. Granerød, M. Leandersson, T. Balasubramanian, and M. Hoesch, Nat. Phys. **10**, 835 (2014).

[5] X. Zhang, Q. Liu, J.-W. Luo, A. J. Freeman, and A. Zunger, Nat. Phys. **10**, 387 (2014).

[6] L. Yuan, Q. Liu, X. Zhang, J. W. Luo, and A. Zunger, Nat. Commun. **10**, 906 (2019).

[7] R. Winkler, *Spin-Orbit Coupling Effects in Two-Dimensional Electron and Hole Systems* (Springer-Verlag, Berlin, Heidelberg, 2003).

[8] H. Yuan, Z. Liu, G. Xu, B. Zhou, S. Wu, D. Dumcenco, K. Yan, Y. Zhang, S.-K. Mo, and P. Dudin, Nano Lett. **16**, 4738 (2016).

[9] W. Jin, P.-C. Yeh, N. Zaki, D. Zhang, J. T. Sadowski, A. Al-Mahboob, A. M. van Der Zande, D. A. Chenet, J. I. Dadap, and I. P. Herman, Phys. Rev. Lett. **111**, 106801 (2013).

[10] J. A. Miwa, M. Dendzik, S. S. Grønborg, M. Bianchi, J. V. Lauritsen, P. Hofmann, and S. Ulstrup, ACS Nano **9**, 6502 (2015).

[11] J. A. Miwa, S. Ulstrup, S. G. Sørensen, M. Dendzik, A. G. Čabo, M. Bianchi, J. V. Lauritsen, and P. Hofmann, Phys. Rev. Lett. **114**, 046802 (2015).

[12] W. Zhao, R. M. Ribeiro, M. Toh, A. Carvalho, C. Kloc, A. Castro Neto, and G. Eda, Nano Lett. **13**, 5627 (2013).

[13] M. M. Ugeda, A. J. Bradley, Y. Zhang, S. Onishi, Y. Chen, W. Ruan, C. Ojeda-Aristizabal, H. Ryu, M. T. Edmonds, and H.-Z. Tsai, Nat. Phys. **12**, 92 (2016).

[14] L. Bawden, S. Cooil, F. Mazzola, J. Riley, L. Collins-McIntyre, V. Sunko, K. Hunvik, M. Leandersson, C. Polley, and T. Balasubramanian, Nat. Commun. **7**, 11711 (2016).

[15] Y. Liu, N. O. Weiss, X. Duan, H.-C. Cheng, Y. Huang, and X. Duan, Nat. Rev. Mater. **1**, 16042 (2016).

[16] H. Zeng, J. Dai, W. Yao, D. Xiao, and X. Cui, Nat. Nano **7**, 490 (2012).

[17] K. F. Mak, K. He, J. Shan, and T. F. Heinz, Nat. Nano **7**, 494 (2012).

[18] F. Bussolotti, H. Kawai, Z. E. Ooi, V. Chellappan, D. Thian, A. L. C. Pang, and K. E. J. Goh, Nano Futures **2**, 032001 (2018).

[19] Y. Zhang, M. M. Ugeda, C. Jin, S.-F. Shi, A. J. Bradley, A. Martín-Recio, H. Ryu, J. Kim, S. Tang, and Y. Kim, Nano Lett. **16**, 2485 (2016).

[20] J. M. Riley, W. Meevasana, L. Bawden, M. Asakawa, T. Takayama, T. Eknapakul, T. Kim, M. Hoesch, S.-K. Mo, and H. Takagi, Nat. Nano **10**, 1043 (2015).

[21] G. Wang, C. Robert, A. Suslu, B. Chen, S. Yang, S. Alamdari, I. C. Gerber, T. Amand, X. Marie, and S. Tongay, Nat. Commun. **6**, 10110 (2015).

[22] R. Suzuki, M. Sakano, Y. Zhang, R. Akashi, D. Morikawa, A. Harasawa, K. Yaji, K. Kuroda, K. Miyamoto, and T. Okuda, Nat. Nano **9**, 611 (2014).

[23] D. Xiao, G.-B. Liu, W. Feng, X. Xu, and W. Yao, Phys. Rev. Lett. **108**, 196802 (2012).

[24] Y. Ye, J. Xiao, H. Wang, Z. Ye, H. Zhu, M. Zhao, Y. Wang, J. Zhao, X. Yin, and X. Zhang, Nat. Nano **11**, 598 (2016).

[25] M. Gehlmann, I. Aguilera, G. Bihlmayer, E. Młyńczak, M. Eschbach, S. Döring, P. Gospodarič, S. Cramm, B. Kardynał, and L. Plucinski, Sci. Rep. **6**, 26197 (2016).

[26] W. Yao, E. Wang, H. Huang, K. Deng, M. Yan, K. Zhang, K. Miyamoto, T. Okuda, L. Li, and Y. Wang, Nat. Commun. **8**, 14216 (2017).

[27] E. Razzoli, T. Jaouen, M.-L. Mottas, B. Hildebrand, G. Monney, A. Pisoni, S. Muff, M. Fanciulli, N. C. Plumb, and V. Rogalev, Phys. Rev. Lett. **118**, 086402 (2017).

[28] A. P. Weber, P. Rüßmann, N. Xu, S. Muff, M. Fanciulli, A. Magrez, P. Bugnon, H. Berger, N. C. Plumb, M. Shi *et al.*, Phys. Rev. Lett. **121**, 156401 (2018).

[29] A. M. Jones, H. Yu, J. S. Ross, P. Klement, N. J. Ghimire, J. Yan, D. G. Mandrus, Y. Wang, and X. Xu, Nat. Phys. **10**, 130 (2014).

[30] L. Qihang, Z. Xiuwen, and Z. Alex, Phys. Rev. Lett. **114**, 661 (2015).

[31] M. Brotons-Gisbert, A. Segura, R. Robles, E. Canadell, P. Ordejón, and J. F. Sánchez-Royo, Phys. Rev. Mater. **2**, 054602 (2018).

[32] P. Li and I. Appelbaum, Phys. Rev. B **97**, 125434 (2018).

[33] J. Jiang, Z. K. Liu, Y. Sun, H. F. Yang, C. R. Rajamathi, Y. P. Qi, L. X. Yang, C. Chen, H. Peng, C. C. Hwang *et al.*, Nat. Commun. **8**, 13973 (2017).

[34] J. R. Schaibley, H. Yu, G. Clark, P. Rivera, J. S. Ross, K. L. Seyler, W. Yao, and X. Xu, Nat. Rev. Mater. **1**, 16055 (2016).

[35] Y. Wang, J. Xiao, H. Zhu, Y. Li, Y. Alsaid, K. Y. Fong, Y. Zhou, S. Wang, W. Shi, Y. Wang *et al.*, Nature **550**, 487 (2017).

[36] D. H. Keum, S. Cho, J. H. Kim, D.-H. Choe, H.-J. Sung, M. Kan, H. Kang, J.-Y. Hwang, S. W. Kim, H. Yang *et al.*, Nat. Phys. **11**, 482 (2015).

[37] S. Cho, S. Kim, J. H. Kim, J. Zhao, J. Seok, D. H. Keum, J. Baik, D.-H. Choe, K. Chang, and K. Suenaga, Science **349**, 625 (2015).

[38] J. A. Wilson and A. D. Yoffe, Adv. Phys. **18**, 193 (1969).

[39] H. K. Dong, S. Cho, J. H. Kim, D. H. Choe, H. J. Sung, K. Min, H. Kang, J. Y. Hwang, S. W. Kim, and H. Yang, Nat. Phys. **11**, 482 (2015).

[40] Y. Zhang, T.-R. Chang, B. Zhou, Y.-T. Cui, H. Yan, Z. Liu, F. Schmitt, J. Lee, R. Moore, Y. Chen *et al.*, Nat. Nano **9**, 111 (2013).

[41] Z. Gong, G.-B. Liu, H. Yu, D. Xiao, X. Cui, X. Xu, and W. Yao, Nat. Commun. **4**,

2053 (2013).

[42] See Supplemental Material at [URL] for detailed information about experimental and theoretical methods, sample synthesis, and additional figures.

[43] M. P. Seah and W. Dench, Surf. Interface Anal. **1**, 2 (1979).

[44] U. Heinzmann and J. H. Dil, J. Phys.: Condens. Matter **24**, 173001 (2012).

[45] J. Osterwalder, J. Phys.: Condens. Matter **24**, 171001 (2012).

[46] J. H. Ryoo and C.-H. Park, Npg Asia Materials **9**, e382 (2017).

[47] S. Cho, J.-H. Park, J. Hong, J. Jung, B. S. Kim, G. Han, W. Kyung, Y. Kim, S. K. Mo, J. D. Denlinger *et al.*, Phys. Rev. Lett. **121**, 186401 (2018).

Acknowledgements

The authors thank Mr. Y. Bian for assistance with the XRD measurements. This work is supported by National Key Research and Development Program of China (Grant No. 2016YFA0300803), the National Natural Science Foundation of China (Grant No. 61427812, 11774160), the Fundamental Research Funds for the Central Universities (Grant No. 021014380113), and Shenzhen Science and Technology Innovation Commission (JCYJ20170818093035338, KQTD20170810105439418, JCYJ20170412110137562, ZDSYS201707271554071). The authors also would like to thank the supports from the Collaborative Innovation Center of Solid State Lighting and Energy-saving Electronics and the Program for high-level Entrepreneurial and

Innovative Talent Introduction, Jiangsu Province.

Captions

FIG. 1 (Color online). (a) Top view and (b) side view of the lattice structure. The upper and lower layers in the unit cell denoted as α and β sectors are inversion partners. (c) Brillouin zone of 2H-$MoTe_2$ in reciprocal space. (d) Raman signal of 2H-$MoTe_2$. A_{1g} and E^1_{2g} denote the phonon modes of 2H-$MoTe_2$. (e) XRD pattern of 2H-$MoTe_2$.

FIG. 2 (Color online). (a) Electronic band structure of 2H-$MoTe_2$ along the high-symmetry points M-K-Γ-M acquired from ARPES. (b), (c) EDC at K and M. Spin splitting of 236 meV at K valley is displayed in (b). (d), (e) Spin polarizations at K (K′) and M. In (d), black and red curves correspond to K and K′, respectively.

FIG. 3 (Color online). (a) Evaluated band structure of bulk 2H-$MoTe_2$ by DFT+SOC. The dotted lines with different colors denote the band projection onto different atomic orbitals, indicating that the first two valence bands (VB1 and VB2 with energy difference of 283 meV) at K point mainly consist of Mo *d*-states. (b), (c) Spin-orbital-projected band structure near K point for the α and β sectors in $MoTe_2$, respectively. The dotted lines with different colors denote the band projection onto different spin and orbit states, with $\uparrow$ ($\downarrow$) indicating the spin projection with the spin polarization axis along the *z* direction and d_{x2-y2} being the majority Mo *d*-state for the plotted bands, illustrating that the inversion partners (α and β sectors) possess opposite local spin polarizations.

FIG. 4 (Color online). (a) Projected local spin polarization for VB1 in the K valley of centrosymmetric 2H-$MoTe_2$. Red (blue) arrows denote the spin polarizations on α (β) sector. (b) Projected local spin polarization of VB2. (c) Spin projection with the spin polarization axis along the *z* direction (S_z) for VB1 and VB2, evaluated from the local spin polarization in bulk 2H-$MoTe_2$ considering the escape depth of photoelectrons. The escape probability of photoelectrons is represented by an exponential function $e^{-\frac{z}{\Delta}}$ with Δ = 6 Å and z being the distance from the sample surface. The black and red squares indicate the spin polarizations (S_z) at K and K′, respectively.

FIG. 5 (Color online). (a) Spin polarization for the first valence band ($VB1_a$) in the K valley of 2H-$MoTe_2$ with a medium dipole field (50 kV/cm) applied along *z* direction to break the inversion symmetry and to split the VB1 (VB2) state in pristine $MoTe_2$ into nearly degenerate $VB1_a$ and $VB1_b$ ($VB2_a$ and $VB2_b$) states for considering broken

inversion symmetry at the surface in experiments. (b) Spin polarization for $VB2_a$. (c), (d) Spin polarizations for $VB1_b$ and $VB2_b$, respectively. (e) Spin projection with the spin polarization axis along the *z* direction (S_z) for $VB1_{a,b}$ (sum of S_z for $VB1_a$ and $VB1_b$) and $VB2_{a,b}$ (sum of S_z for $VB2_a$ and $VB2_b$), evaluated using the same method as in Fig. 4(c) for comparison. The black and red squares indicate the spin polarizations (S_z) at K and K′, respectively.

FIG. 1

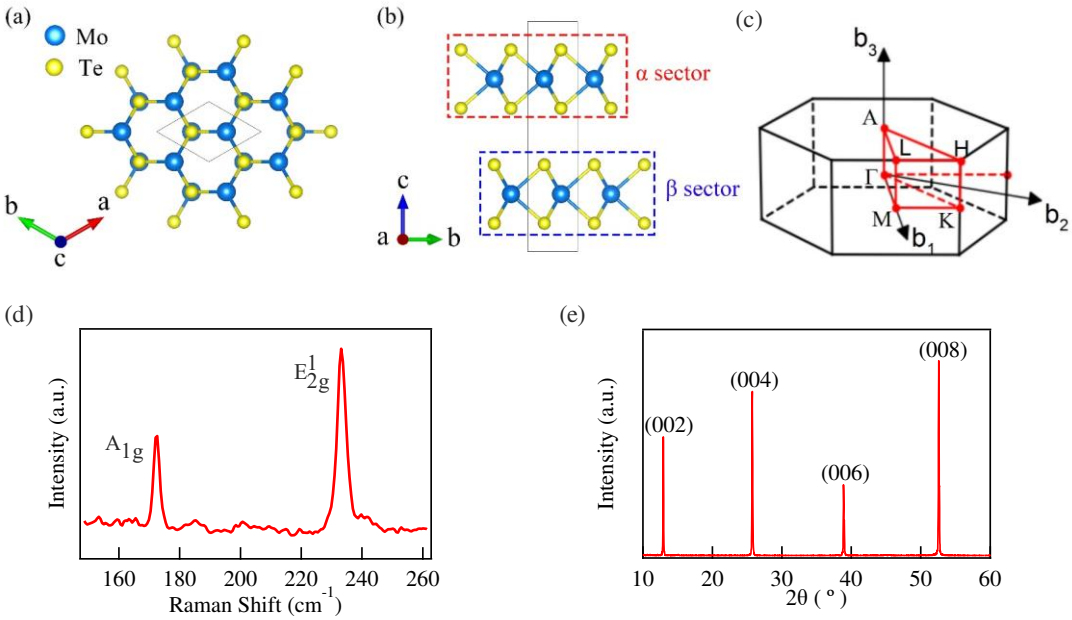

FIG. 2

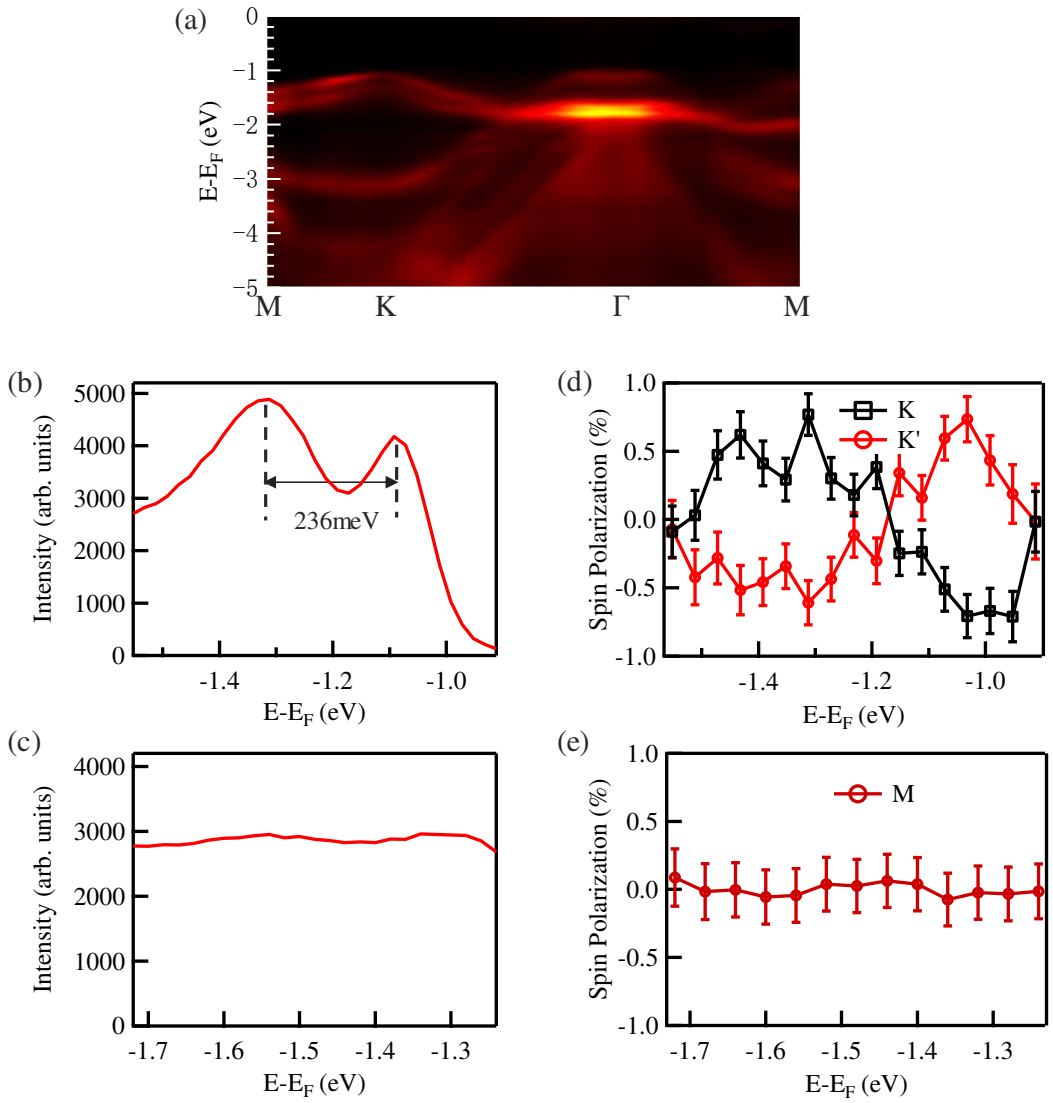
(a)
0
−1
−2
−3
−4
−5
E-E$_F$ (eV)
M
K
Γ
M
(b)
Intensity (arb. units)
5000
4000
3000
2000
1000
0
236meV
-1.4
-1.2
-1.0
E-E$_F$ (eV)
(c)
Intensity (arb. units)
4000
3000
2000
1000
0
-1.7
-1.6
-1.5
-1.4
-1.3
E-E$_F$ (eV)
(d)
Spin Polarization (%)
1.0
0.5
0.0
-0.5
-1.0
K
K'
-1.4
-1.2
-1.0
E-E$_F$ (eV)
(e)
Spin Polarization (%)
1.0
0.5
0.0
-0.5
-1.0
M
-1.7
-1.6
-1.5
-1.4
-1.3
E-E$_F$ (eV)

FIG. 3

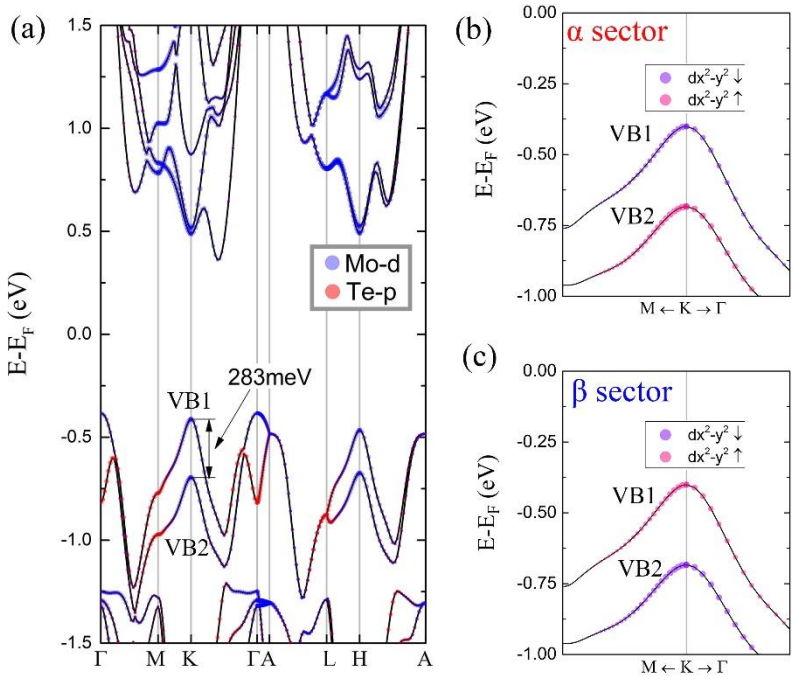
(a)
(b)
(c)
α sector
β sector
Mo-d
Te-p
283meV
VB1
VB2
E-E$_F$ (eV)
Γ M K ΓA L H A
M ← K → Γ
dx^2-y^2 ↓
dx^2-y^2 ↑

FIG. 4

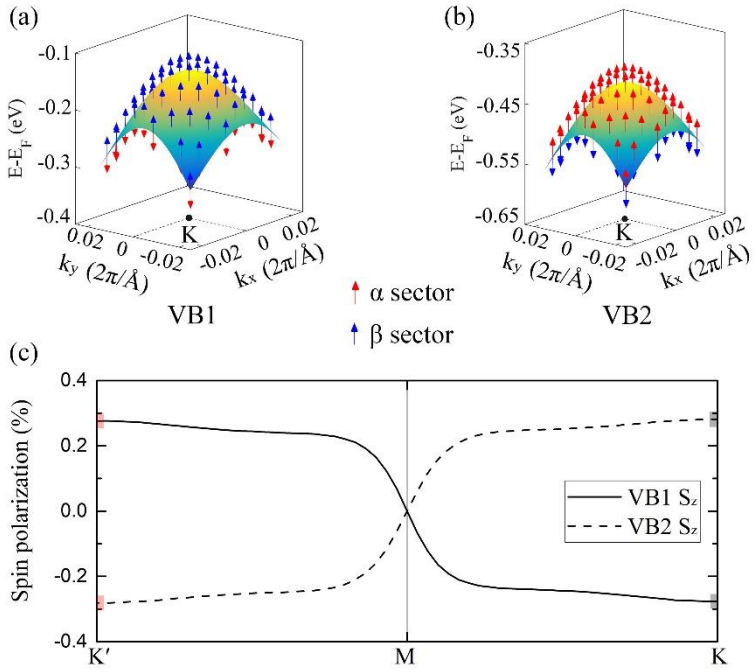
(a)
-0.1
-0.2
-0.3
-0.4
E-E$_F$ (eV)
K
0.02 0 -0.02
k_y (2π/Å)
-0.02 0 0.02
k_x (2π/Å)
VB1
(b)
-0.35
-0.45
-0.55
-0.65
E-E$_F$ (eV)
K
0.02 0 -0.02
k_y (2π/Å)
-0.02 0 0.02
k_x (2π/Å)
VB2
α sector
β sector
(c)
0.4
0.2
0.0
-0.2
-0.4
Spin polarization (%)
VB1 S_z
VB2 S_z
K′
M
K

FIG. 5

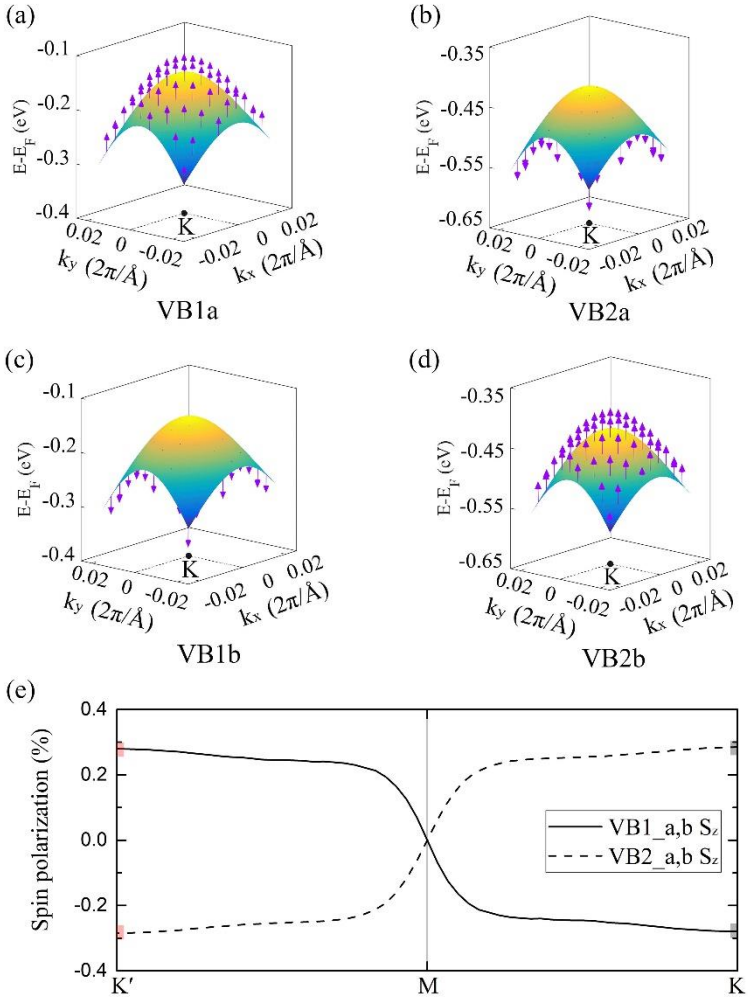
(a)
-0.1
-0.2
-0.3
-0.4
E-E_F (eV)
K
0.02 0 -0.02
k_y (2π/Å)
-0.02 0 0.02
k_x (2π/Å)
VB1a
(b)
-0.35
-0.45
-0.55
-0.65
E-E_F (eV)
K
0.02 0 -0.02
k_y (2π/Å)
-0.02 0 0.02
k_x (2π/Å)
VB2a
(c)
-0.1
-0.2
-0.3
-0.4
E-E_F (eV)
K
0.02 0 -0.02
k_y (2π/Å)
-0.02 0 0.02
k_x (2π/Å)
VB1b
(d)
-0.35
-0.45
-0.55
-0.65
E-E_F (eV)
K
0.02 0 -0.02
k_y (2π/Å)
-0.02 0 0.02
k_x (2π/Å)
VB2b
(e)
0.4
0.2
0.0
-0.2
-0.4
Spin polarization (%)
VB1_a,b S_z
VB2_a,b S_z
K′
M
K